Nano Research

Open Access

Research Article

Oxygen nanobubbles of ICG dimers achieve self-cascade photothermal and photodynamic therapy for hypoxia-reversible tumor treatment

Xiang Sun[1], Zheng Zhang[2], Moran Wang[1], Yuqin Chen[1], Xiang Meng[1], Wenjun Zhao[1], Juan Jin[1], Wanghanqi Yang[1], Chengwan Xia[2] ✉, Yuxin Wang[2], Shengliang Li[3] ✉, Bin Huang[1] ✉, and Ning Gu[1,4] ✉

[1] *Key Laboratory for Bio-Electromagnetic Environment and Advanced Medical Theranostics, School of Biomedical Engineering and Informatics, Nanjing Medical University, Nanjing 210029, China*
[2] *Department of Oral and Maxillofacial Trauma Orthognathic Plastic Surgery, Nanjing Stomatological Hospital, Research Institute of Stomatology, Medical School of Nanjing University, Nanjing 210093, China*
[3] *College of Pharmaceutical Sciences, Soochow University, Suzhou 215123, China*
[4] *Nanjing Key Laboratory for Cardiovascular Information and Health, Engineering Medicine Institute of Clinical Medicine, Nanjing Drum Tower Hospital, Medical School of Nanjing University, Nanjing 210008, China*

Cite this article: *Nano Research*, **2025**, *18*, 94907281. https://doi.org/10.26599/NR.2025.94907281

ABSTRACT: Simultaneous photothermal and photodynamic therapies (PTT and PDT) hold great promise for noninvasive tumor therapy. However, effective regulation of PTT and PDT with optimal synergistic effects remains a challenge. To date, there are only a few synergistic PTT and PDT methods with suitable collaborative effects due to the rarity of efficient nanoplatforms with good cascading properties. To overcome this limitation, a proof-of-concept of self-cascade PTT and PDT was developed for hypoxia-reversible tumor therapy. With the assembly of dimeric indocyanine green (DICG) with oxygen nanobubbles (O_2-NBs), DICG/O_2-NBs typically exhibit J-aggregates for significant PTT effects, with a high photothermal conversion efficiency of 51.45% under 880 nm light irradiation. Interestingly, the PTT performance of DICG/O_2-NBs can switch J-aggregates of DICG into DICG monomers with efficient O_2 gas liberation, while producing hydroxyl radicals for type I PDT. Additionally, the evolved DICG monomer reacts with the released O_2 to generate plenty of $^1O_2$ for efficient type II PDT. With these advantages, the cascaded nanoplatform achieves good tumor targeting and biocompatibility, and thus has high tumor inhibition of 94.26%, with an obvious ability to reverse hypoxia. This work demonstrates the efficiency of self-cascade PTT and PDT nanomedicine for high-performance hypoxia-reversible tumor ablation, thus providing a new approach for the development of cascading phototheranostics *in vivo*.

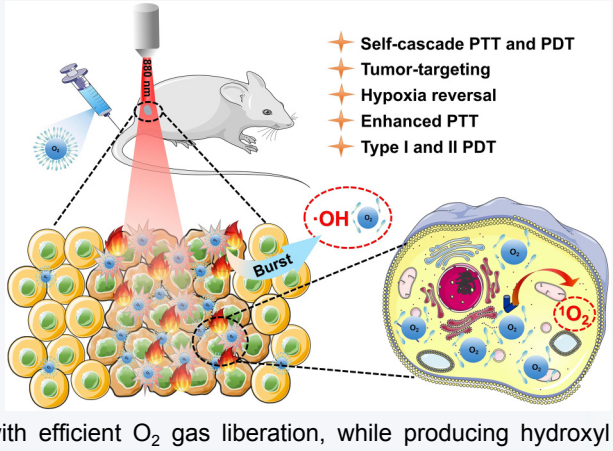

KEYWORDS: indocyanine green (ICG) dimer, oxygen nanobubble, J-aggregate, self-cascade, photothermal therapies (PTT), photodynamic therapies (PDT)

1 Introduction

As an emerging noninvasive means of tumor therapy, optical diagnosis and treatment technology, represented by photothermal and photodynamic therapies (PTT and PDT), has attracted widespread attention in recent years [1–8]. In general, PTT uses a photosensitizer to convert external laser light to heat to eliminate target cancer cells [9]. However, PTT at high temperatures (> 55 °C) damages normal tissue near the tumor, whereas reducing the treatment temperature (< 43 °C) affects the treatment effect [10]. In contrast, PDT uses a photosensitizer under appropriate laser irradiation to generate reactive oxygen species (ROS) such as singlet oxygen ($^1O_2$), hydroxyl radical (·OH), superoxide anions and

Received: December 21, 2024; **Revised:** January 25, 2025
Accepted: February 2, 2025

✉Address correspondence to Ning Gu, guning@nju.edu.cn; Bin Huang, huangbinhb31@njmu.edu.cn; Shengliang Li, lishengliang@suda.edu.cn; Chengwan Xia, Xiachengwan@163.com

so on, which destroy various biomacromolecules in tumor cells via oxidation reactions and produce cytotoxic effects [11–13]. Unfortunately, the hypoxic environment of tumors can affect the efficacy of PDT [14]. To overcome the limitations of single PTT or PDT, researchers have combined PTT and PDT, which shows great potential in enhancing the synergistic effects of tumor treatment [15–17]. However, both photothermal and photodynamic processes involve the utilization of the excited state of the photosensitizer. Simultaneous PTT and PDT inevitably cause energy competition, thus limiting their therapeutic effects. Thus far, increasing the therapeutic benefits of PDT and PTT during the treatment of tumors is still highly challenging.

Cascade catalysis and reactions are of great interest in many fields, such as biological enzyme catalysis and chemical manufacturing [18, 19]. Recently, several efficient cascade catalysts have been developed, stimulating further development in academic and industrial fields [20]. Inspired by breakthroughs in cascade catalysis and reactions, designing cascade PTT and PDT to avoid competing for the excited state of a photosensitizer has yet to be realized but is fantastically important for fundamental and applied research on optical diagnosis and treatment technology. To achieve cascade PDT and PTT, the key lies in the design of the material system. Although some photosensitizers showing simultaneous PTT and PDT have been reported [21, 22], there are no reports on photosensitizers exhibiting cascade PTT and PDT.

Compared with complex molecular synthesis and modification processes, the aggregation regulation of near-infrared (NIR) photosensitizers (PSs) as a facile and flexible pathway has gained increasing attention in recent years [23]. In particular, J-aggregates (that is, molecules displaying highly ordered "head-to-tail" stacking) of some NIR PSs exhibit excellent photophysical properties, such as redshifted absorption and emission and increased extinction coefficients [24, 25]. On the other hand, J-aggregates may be destroyed in response to heat, solvents, laser irradiation, etc [26]. More importantly, along with the destruction of J-aggregates into free monomers, their optical properties change accordingly, which may in turn lead to the transformation of treatment modalities. J-aggregates of NIR PSs may provide support for the construction of cascade PTT and PDT material systems.

Compared with indocyanine green (ICG), the only clinically available NIR dye approved by the U.S. Food and Drug Administration [27–31], dimeric indocyanine green (DICG) exhibits enhanced PTT [32]. In this work, J-aggregates of DICG (DICG(J)) and monomers of DICG (DICG(M)) were found to have single PTT and PDT performances, respectively. Notably, oxygen nanobubbles (O_2-NBs) have great potential for improving the hypoxic environment [33, 34] and enhancing the PDT effect [35, 36]. Herein, we propose a proof-of-concept of self-cascade PTT and PDT for hypoxia-reversible tumor therapy (Fig. 1). We have successfully developed a self-cascade PTT and PDT system, DICG/O_2-NBs, which is fabricated by the assembly of DICG with O_2-NBs. DICG/O_2-NBs exhibit typical J-aggregates with significant PTT effects upon irradiation with 880 nm light. The PTT effects of DICG/O_2-NBs can readily convert DICG(J) into DICG(M) with efficient O_2 gas liberation, while producing ·OH for type I PDT. Additionally, the evolved DICG monomer reacts with the released O_2 to generate plenty of $^1O_2$ for efficient type II PDT. Owing to these merits, the cascaded nanoplatform achieves good tumor targeting and biocompatibility, obvious hypoxia reversal, and high tumor inhibition *in vivo*.

2 Experimental

2.1 Preparation of DICG(J)/O_2-NBs

ICG (10 mg) was dissolved in 10 mL of deionized water. The resulting solution was heated in a water bath at 80 °C and stirred at 800 rpm for 10 h. After cooling to room temperature, a dark green mixture was obtained and diluted to 100 μg/mL. A small amount of the sample was concentrated for ^{1}H nuclear magnetic resonance (NMR) analysis (Fig. S1 in the Electronic Supplementary Material (ESM), [37]). The diluent (2 mL) is subsequently transferred into a 3 mL penicillin bottle with a medical syringe filled with 3 mL O_2 gas. Afterwards, DICG(J)/O_2-NBs were generated via the repeated compression method [38]. The preparation control device is shown in Fig. S2 in the ESM.

2.2 Characterization

The hydrodynamic diameters and zeta potentials of DICG(J) and DICG(J)/O_2-NBs solution were measured via dynamic light scattering (DLS) on a laser nanosize analyser (Litesizer 500, Anton Paar) at room temperature. The concentrations of particles in DICG(J) and DICG(J)/O_2-NBs solutions were measured on a NanoCoulter counter (Resun-E03, Resun Technology, China). Morphology images of the samples were taken via transmission electron microscopy (FEI Tecnai G2). The ultraviolet–visible–near infrared spectroscopy (UV–Vis–NIR) absorbance spectra (300 to 1000 nm) of the samples were recorded on a spectrophotometer (Cary 5000, Agilent). The oxygen contents in the deionized water, DICG(J) and DICG(J)/O_2-NBs solution were analysed with a dissolved oxygen meter (JPSJ-606T, Shanghai Yidian Scientific Instruments Co., Ltd., China).

2.3 Photothermal effect

To evaluate the photothermal effects of the samples, two NIR laser sensors (LR-MFJ-880 and LR-MFJ-808, Changchun Leirui Photoelectric Technology Co., Ltd.) were used in the experiment. For the photothermal tests, the samples were transferred into a 3 mL quartz vial and illuminated with NIR lasers (ICG: $\lambda_{808\ nm}$; DICG: $\lambda_{880\ nm}$). The temperature changes of the samples during irradiation were recorded through heat images every minute via an infrared thermal imaging camera (FLK-Ti400U, Fluke, USA).

2.4 ROS production

The amount of ROS produced was determined via the use of 2',7'-dichlorofluorescein (DCFH) as an indicator. The fluorescence intensity of DCFH (excitation wavelength: 488 nm, emission wavelength: 525 nm) was determined with a fluorescence spectrophotometer (FS5, Edinburgh). The amount of $^1O_2$ generated was evaluated via 1,3-diphenylisobenzofuran (DPBF) as a detection probe. Typically, ICG, DICG(J), DICG(M), DICG(J)/O_2-NBs, and DICG(M)/O_2-NBs solution (10 μg/mL) were placed in 3 mL quartz vials in the presence of 100 μL of DPBF solution (0.5 mg/mL, freshly dissolved in dimethyl sulfoxide (DMSO)). In the case of ICG, DICG(M) and DICG(M)/O_2-NBs, irradiation was conducted with NIR lasers (ICG: $\lambda_{808\ nm}$; DICG: $\lambda_{880\ nm}$) at 1 W/cm^2 for 150 s. To prevent the conversion of DICG(J) to DICG(M), irradiation is conducted with an NIR laser (880 nm, 0.1 W/cm^2) for DICG(J) and DICG(J)/O_2-NBs. During irradiation, the UV–Vis spectra of the mixture were recorded via a UV–Vis–NIR spectrophotometer (Cary 5000, Agilent) at 420 nm.

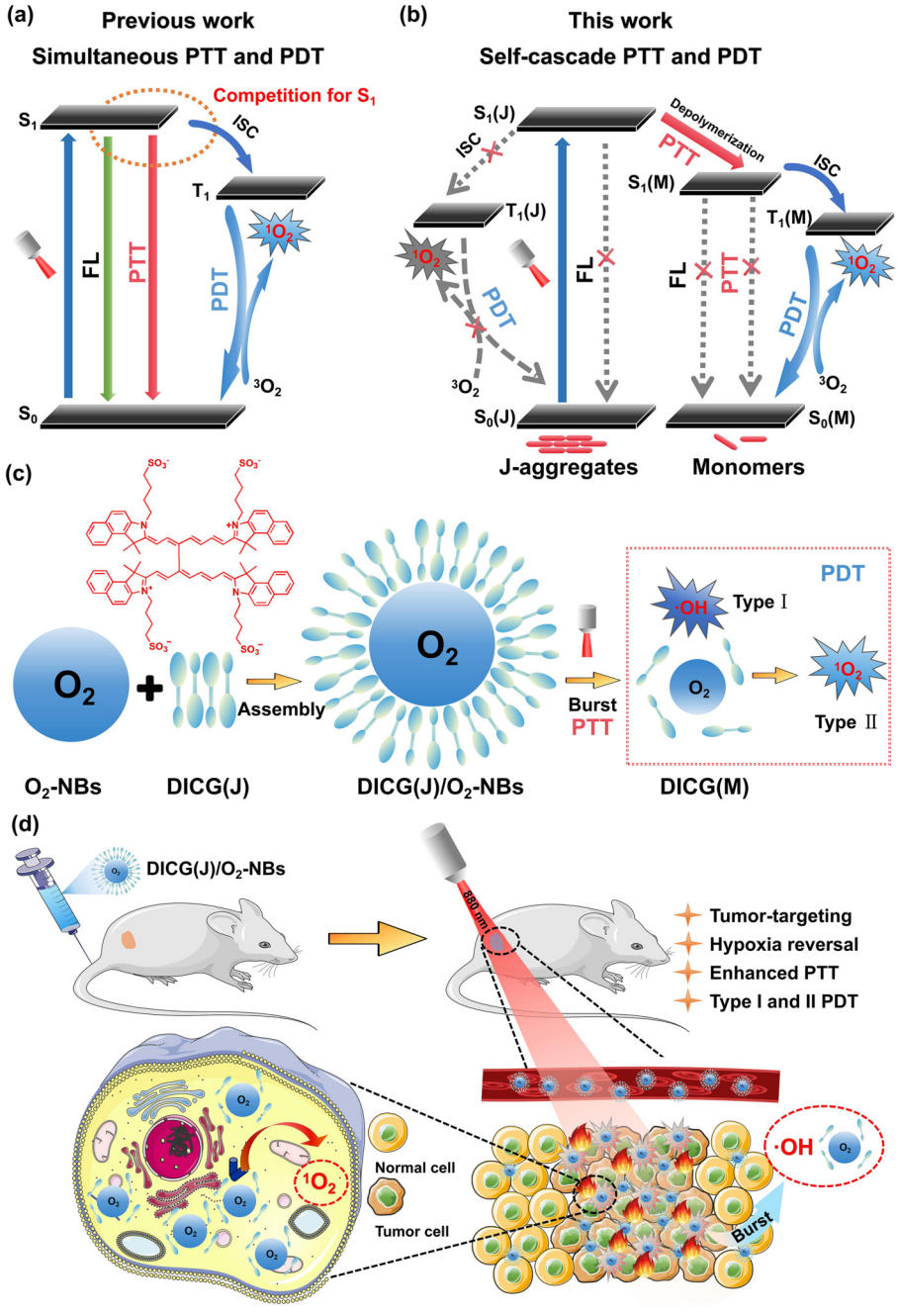

Figure 1 (a) Mechanism of simultaneous PTT and PDT. (b) Mechanism of cascade PTT and PDT. (c) Schematic illustration of a light-triggered cascade PTT and PDT system based on DICG(J)/O_2-NBs. (d) Schematic illustration of a light-triggered DICG(J)/O_2-NBs system for self-cascade PTT and PDT *in vivo*.

2.5 Cell culture, uptake and cytotoxicity

Cal27 human tongue cancer cells were purchased from the American Type Culture Collection (Manassas, VA, USA). The cells were grown in Dulbecco's modified Eagle's medium supplemented with streptomycin (100 mg/mL), 1% penicillin, and 10% fetal bovine serum at 37 °C under a 5% CO_2 atmosphere in a humid incubator. The cell culture medium was replaced every 48 h. Fluorescence images of the cells were taken via confocal laser scanning microscopy (CLSM, FV3000, Olympus).

The confocal culture dishes were seeded with Cal27 cells at a density of 1×10^5 cells per well and incubated for 24 h at 37 °C with 5% CO_2. Next, the cells were washed with phosphate-buffered saline (PBS, pH 7.4) three times, treated with 100 μL DICG(J) or DICG(J)/O_2-NBs solution with the same DICG concentration (10 μg/mL) and incubated for 12 h. For the cell uptake test, the cells were washed with PBS three times, fixed with 4% paraformaldehyde (1 mL) for 20 min, and then stained with 4,6-diamidino-2-phenylindole (DAPI, 100 μL) for 15 min. For ROS detection, the cells were washed with PBS, incubated with 2',7'-dichlorofluorescein diacetate (DCFH-DA, 10 μM, 1 mL) for 20 min, and irradiated with a laser at a wavelength of 880 nm and a power density of 1 W/cm^2 at room temperature for 5 min. Finally, the cells were washed with PBS (three times) and immediately imaged via CLSM.

Cal27 cells were inoculated in 96-well plates at a density of 1 ×

10^4 per well and cultured in a standard cell incubator for 24 h. Then, the cells were washed with PBS three times and treated with DICG(J) and DICG(J)/O_2-NBs solutions at different concentrations. After further incubation for 12 h, upon laser irradiation (1 W/cm², 880 nm, 5 min) or without laser irradiation, the cells were inoculated overnight and washed with PBS (three times), and the metabolic activity of the cells was detected via a cell counting kit-8 (CCK-8) assay.

2.6 Animal experiments

All animal experiments were conducted in accordance with the guidelines of the Animal Core Facility of Nanjing Medical University and were approved by the Institutional Animal Care and Use Committee of Nanjing Medical University (IACUC 202406030). Male BALB/c nude mice and BALB/c mice (5 weeks of age) were obtained from the Animal Core Facility of Nanjing Medical University. Cal27 cells (2×10^8 cells per mL, 100 μL) were implanted via subcutaneous injection into nude mice to establish a tumor model. The antitumour efficacy assay was conducted when the tumor volume was approximately 30 mm³. To evaluate the targeting and enrichment ability of DICG, the tumor-bearing mice were intravenously injected with 100 μL of fluorescein isothiocyanate-dextran (2.5 mg/mL) and 100 μL of DICG(J) solution (100 μg/mL) into the tail vein. After 5 min, the fluorescence signals in the tumor and major organs, such as muscle and liver, were recorded on a dual-modality small animal *in situ* cell analysis imaging system (IVM-CMS3, IVIM Technology, Korea). Twelve mice were allocated to four groups at random: (1) the PBS group (each mouse was injected with 100 μL of PBS without irradiation), (2) the DICG(J) group (each mouse was injected with 100 μL of 100 μg/mL DICG(J) without irradiation), (3) the DICG(J) plus laser group (each mouse was irradiated with a laser (880 nm, 1 W/cm²) for 10 min after injection of 100 μL of 100 μg/mL DICG solution), and (4) the DICG(J)/O_2-NBs plus laser group (each mouse was irradiated with a laser (880 nm, 1 W/cm²) for 10 min after injection of 100 μL of 100 μg/mL DICG(J)/O_2-NBs).

During antitumour therapy, a thermographic camera was used to record the temperature changes at the irradiation sites continuously. The oxygen saturation of hemoglobin in Cal27 tumor-bearing nude mice was investigated via a perfusion and oxygenation imager (MoorO$_2$Flo-2, Moor Instruments Ltd.). All the mice were treated twice on days 1 and 4. No treatment was administered for the final 8 days of the experiment. The tumor volume and body weight were measured every 2 days during the treatment. The tumor volumes were calculated as length × (width)²× 0.52. After therapy, the major organs (heart, liver, spleen, lung, and kidney) and tumors were harvested from the mice. The organs and tumors were sliced and stained via hematoxylin and eosin (H&E). Additionally, tumor immunofluorescence was performed to analyse the levels of the hypoxia-inducible factor-1α (HIF-1α) and nuclear factor (erythroid-derived 2)-like 2 (Nrf2) induction factors. Finally, the slices were observed and photographed via a digital microscope for histological analysis.

2.7 Biocompatibility

To evaluate the biocompatibility of DICG(J)/O_2-NBs, healthy BALB/c mice were selected for the experiment. After continuous tail intravenous injection of DICG(J)/O_2-NBs (100 μL of 100 μg/mL every day) for 3 days, blood samples were taken via the cardiac blood collection method for hematological analysis. Blood samples from untreated rats were used as controls. To evaluate the immune response and potential cytotoxicity, biological parameters, including white blood cell (WBC) count, red blood cell (RBC) count, hemoglobin (HGB) count, platelet (PLT) count, platelet accumulation (PCT), mean corpuscular volume (MCV), mean corpuscular hemoglobin (MCH), mean corpuscular hemoglobin concentration (MCHC), red cell distribution width (RDW), mean platelet volume (MPV), and lymphocyte (Lymph) count were analysed.

3 Results and discussion

3.1 Preparation and characterization

DICG was facilely synthesized via a one-pot reaction via heat treatment (Fig. 2(a)). The absorbance of the reaction mixture was measured (Fig. 2(b)). The initial solution exhibited two major absorption peaks at 700 and 780 nm, which can be attributed to the typical absorption of ICG [31]. With the dimerization of ICG and the formation of DICG(J), the absorption peak of the solution gradually decreased at 700 and 780 nm, whereas the absorption peak at 895 nm increased. At 10 h, three characteristic absorption peaks at 680, 780 and 895 nm did not change, indicating the end of the reaction. The structure of DICG was confirmed by ^{1}H NMR (Fig. S1 in the ESM). In methanol-D4 (MeOD), ICG displays two proton signals at 6.40 and 6.65 ppm, corresponding to $H^{\alpha,\alpha'}$ and $H^{\gamma,\gamma'}$ of the alkyne chain, respectively. In contrast, the proton signals shift to 5.90 (H^{α}) and 6.50 ($H^{\alpha',\gamma'}$) ppm, confirming the formation of the *γ*-*γ* dimer DICG [37]. The absorption spectra (Fig. S3 in the ESM) of DICG aqueous solution (1 mg/mL) did not change significantly within 6 days at room temperature, indicating good stability.

DICG(J)/O_2-NBs were successively prepared via the repeated compression method according to our previous report [38]. The hydrodynamic diameters and Zeta potentials of DICG(J) and DICG(J)/O_2-NBs solutions were measured via DLS. The average hydrodynamic sizes of DICG(J) and DICG(J)/O_2-NBs were measured to be 200 and 300 nm with polydispersity indices of 0.26 and 0.30 (Fig. 2(c), and Fig. S4 in the ESM), respectively. The nanoparticle concentrations of DICG(J) and DICG(J)/O_2-NBs were determined to be 1.01×10^{10} and 1.35×10^{10} particles/mL (Fig. S5 in the ESM), respectively. Transmission electron microscopy (TEM) images revealed that DICG(J) and DICG(J)/O_2-NBs (Figs. 2(d) and 2(e)) had spherical shapes with average diameters of 100 and 150 nm, respectively. The smaller sizes of DICG(J) and DICG(J)/O_2-NBs obtained from the TEM measurements can be attributed to the shrinkage of the hydrating layer. The average Zeta potentials are estimated to be −22.23 and −31.19 mV for DICG(J) and DICG(J)/O_2-NBs (Fig. 2(f)), respectively, reflecting good colloidal stability.

As a key parameter, the dissolved oxygen content of the samples was also assessed. As illustrated in Fig. 2(g), the oxygen content of the DICG(J)/O_2-NBs solution was estimated to be 30.69 mg/L, which was 3.65 times greater than that of the DICG(J) solution (8.40 mg/L). The high oxygen content suggests that DICG(J)/O_2-NBs are beneficial for improving the hypoxic environment and hold considerable potential for PDT. Furthermore, the DICG(J) solution was treated with MeOH to obtain DICG(M). With the addition of MeOH, the typical absorption peak of DICG(J) at 895 nm disappears, whereas the absorption peak at 780 nm appears (Fig. 2(h)), indicating the transformation of DICG(J) to DICG(M)

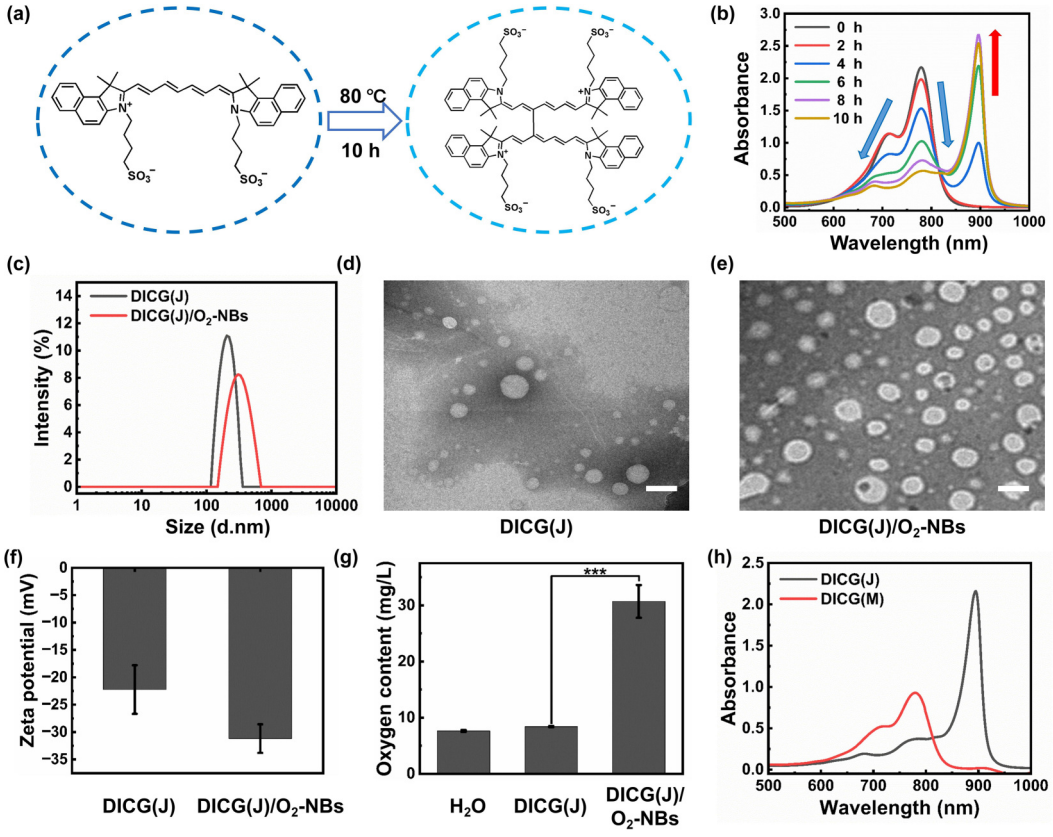

Figure 2 (a) Synthesis route of DICG. (b) Changes in the absorbance of the reaction mixture with time. (c) DLS analysis of DICG(J) and DICG(J)/O_2-NBs solution. (d) TEM image of DICG(J). (e) TEM image of DICG(J)/O_2-NBs. (f) Zeta potential of DICG(J) and DICG(J)/O_2-NBs solution. (g) Oxygen content of the deionized water, DICG(J) and DICG(J)/O_2-NBs solution. (h) Absorbance spectra of DICG(J) and DICG(M). The error bars represent the standard error (mean ± SEM, n = 3). The values are presented as the means ± SEMs, $^{***}P < 0.001$. Scale bars: 200 nm.

[32]. The fluorescence emission spectra of the samples were also examined. In comparison with ICG, DICG(J) and DICG(M) solutions show extremely low emission (Fig. S6 and Table S1 in the ESM), indicating that the relaxation of the excited state is mainly via nonradiative pathways and enables PTT and PDT in DICG.

3.2 Photothermal effect

The photothermal properties of the samples were investigated. As shown in Figs. 3(a) and 3(b), after 10 min of laser irradiation (1.0 W/cm^2; $\lambda_{808\ nm}$ for ICG; $\lambda_{880\ nm}$ for DICG), the temperature increases by 29.0, 27.8 and 26.5 °C for DICG(J)/O_2-NBs, DICG(J) and ICG solutions, respectively, indicating that the photothermal conversion performances of DICG(J)/O_2-NBs and DICG(J) are similar and superior to those of ICG. This is mainly due to the J-aggregate structures of DICG(J)/O_2-NBs and DICG(J). In sharp contrast, the temperature changes are only 7.2 and 7.4 °C for DICG(M) and DICG(M)/O_2-NBs, respectively, suggesting the insignificant PTT effect of DICG(M). The obvious difference in the photothermal conversion performance between J-aggregates and free monomers of DICG provides the possibility of switching treatment modes.

The photothermal effects of DICG(J)/O_2-NBs at different concentrations were also evaluated (Fig. 3(c), and Fig. S7(a) in the ESM). At a low concentration of 50 μg/mL, the temperature rise of DICG(J)/O_2-NBs is only 23.1 °C. As the concentration increased to 100 μg/mL or even higher, the DICG(J)/O_2-NBs solution exhibited similar photothermal effects, with a temperature increase of 29.0–31.3 °C. As a result, 100 μg/mL is the preferred concentration for PTT. Next, the photothermal properties of DICG(J)/O_2-NBs were tested by varying the light irradiance fluence. With increasing laser power from 0.5 to 2.0 W/cm^2, the temperature increased from 16.5 to 39.8 °C (Fig. 3(d), and Fig. S7(b) in the ESM). With security in mind, 1.0 W/cm^2 was selected for the next treatment. Furthermore, the influence of the photothermal response was characterized by "On/Off" irradiation cycles (Fig. 3(e)). The temperature increase of the DICG(J)/O_2-NBs and DICG(J) solutions are 34.6 °C. The photothermal conversion efficiencies of DICG(J)/O_2-NBs and DICG(J) were calculated to be 51.45% and 51.34% (Fig. 3(f) and Fig. S8 in the ESM), respectively. The results demonstrate that DICG(J)/O_2-NBs have photothermal conversion properties similar to those of DICG(J).

Figures 3(g) and 3(h) reveal that the typical absorption peak of DICG(J) and DICG(J)/O_2-NBs at 895 nm gradually decreases during laser irradiation, whereas a new absorption peak appears at 780 nm, which can be ascribed to the absorption of DICG(M). The absorption change confirms the transformation of DICG(J) to DICG(M) in response to laser irradiation. Meanwhile, the oxygen content of the DICG(J)/O_2-NBs solution decreases from 30.69 to 24.22 mg/L with laser irradiation (Fig. S9 in the ESM), which is beneficial for overcoming the hypoxic environment. Compared with DICG(J), DICG(J)/O_2-NBs have a faster degradation rate, which favours the construction of a light-triggered self-cascade system.

A photothermal experiment was performed with 880 nm laser

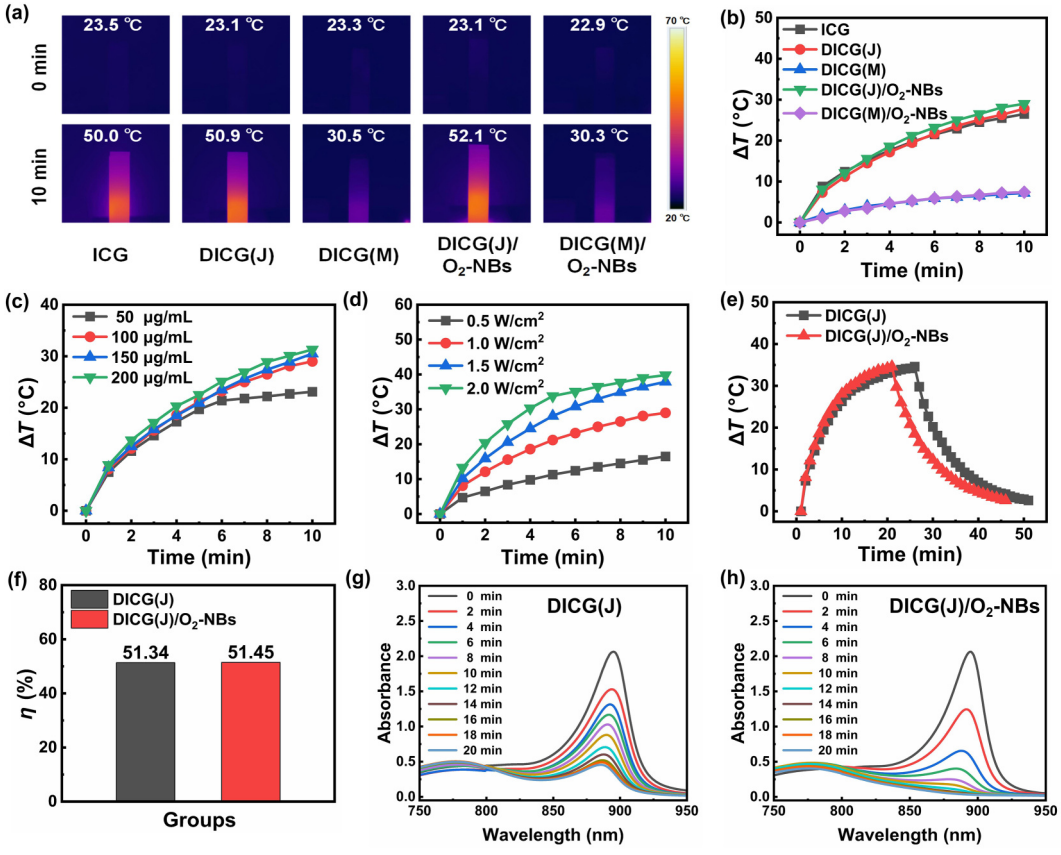

Figure 3 Photothermal response of the samples upon irradiation (880 nm for DICG and 808 nm for ICG). (a) Thermal images, (b) temperature change versus time plot for ICG, DICG(J), DICG(M), DICG(J)/O_2-NBs, and DICG(M)/O_2-NBs at 100 μg/mL in H_2O when irradiated with a laser (1 W/cm^2) for 10 min. (c) Temperature change versus time plot for DICG(J)/O_2-NBs with different concentrations (i.e., 50, 100, 150, and 200 μg/mL) when irradiated with a laser (1 W/cm^2) for 10 min. (d) Temperature versus time plot for DICG(J)/O_2-NBs upon irradiation at 100 μg/mL for 10 min at irradiances of 0.5, 1.0, 1.5, and 2.0 W/cm^2. (e) Temperature profiles of DICG(J)/O_2-NBs and DICG(J) solutions under irradiation for two consecutive on/off cycles. (f) Photothermal conversion efficiencies of DICG(J)/O_2-NBs and DICG(J). (g) Absorption changes of DICG(J) and (h) DICG(J)/O_2-NBs in response to laser irradiation.

irradiation from 0–5 min and 808 nm laser irradiation from 6–10 min. The results found a slight change in the temperature increase (Fig. S10 in the ESM). These results suggest that changing the irradiation wavelength of NIR may mildly affect the PTT effect. Although the absorption of DICG//O_2-NBs at 880 nm was low ($A_{880\ nm}$ = 0.17) at 10 min (Fig. 3(h)), the DICG//O_2-NBs held a relative high absorbance coefficient (2.73 × 10^4 L/(mol·cm)) for PDT. Thus, 880 nm laser irradiation is chosen for the following *in vitro* and *in vivo* experiments.

3.3 ROS production

The ROS production capacity of the samples was determined via the use of DCFH as a probe. As illustrated in Figs. 4(a) and 4(b), the fluorescence intensity measured at 525 nm revealed that the ROS generation of DICG(M)/O_2-NBs significantly improved after 10 min of laser irradiation, and its peak fluorescence intensity was 4.2-fold greater than that of DICG(M) alone. The significant increase in ROS generation is attributed mainly to the instability of DICG(J)/O_2-NBs in response to laser irradiation. Owing to the increase in temperature, DICG(J)/O_2-NBs detonate and liberate O_2 gases and DICG(M) while producing many ·OH molecules, which are considered ROS for type I PDT. Moreover, DICG(M) reacts with liberative O_2 gases to form $^1O_2$ for type II PDT. Subsequently, DPBF was employed as an indicator to evaluate the $^1O_2$ generation capacity of the samples. The time-dependent absorption of DPBF was recorded upon laser irradiation. As illustrated in Figs. 4(c)–4(e), after irradiation for 150 s, the absorbance intensity of DPBF (420 nm) remained at 0.94, 0.96, and 0.87 of the initial values for ICG, DICG(J) and DICG(M), respectively, suggesting a negligible decrease with time. In contrast, in the cases of DICG(J) and DICG(M) assembled with O_2-NBs, the absorbance intensities of DPBF rapidly decrease to 0.94 and 0.53 of the original values (Figs. 4(f) and 4(g)), respectively. For better contrast, the time-dependent absorption changes at 420 nm of DPBF induced by different samples are summarized in Fig. 4(h). These results indicate that the assembly of DICG with O_2-NBs can significantly increase $^1O_2$ generation, which can be attributed to the remarkable increase in the oxygen concentration, promoting the reaction between triplet DICG and oxygen.

As shown in Fig. 4(i), the $^1O_2$ quantum yields of the samples were calculated (Fig. S11 and Table S1 in the ESM). The $^1O_2$ quantum yields of DICG(J), DICG(M), DICG(J)/O_2-NBs, and DICG(M)/O_2-NBs are calculated to be 0.23%, 0.88%, 0.06%, and 3.37%, respectively. Among these samples, DICG(M)/O_2-NBs have the largest $^1O_2$ quantum yield, which is approximately 17 times greater than that of ICG (0.20%) [36], indicating high PDT potential. Compared with ICG/O_2-NBs [36] and other ICG derivatives [39], DICG(M)/O_2-NBs also show higher $^1O_2$ quantum yield. Note that DICG(J) can be transformed to DICG(M) upon laser irradiation, and DICG(J)/O_2-NBs are expected to be an ideal system for achieving self-cascade PTT and PDT.

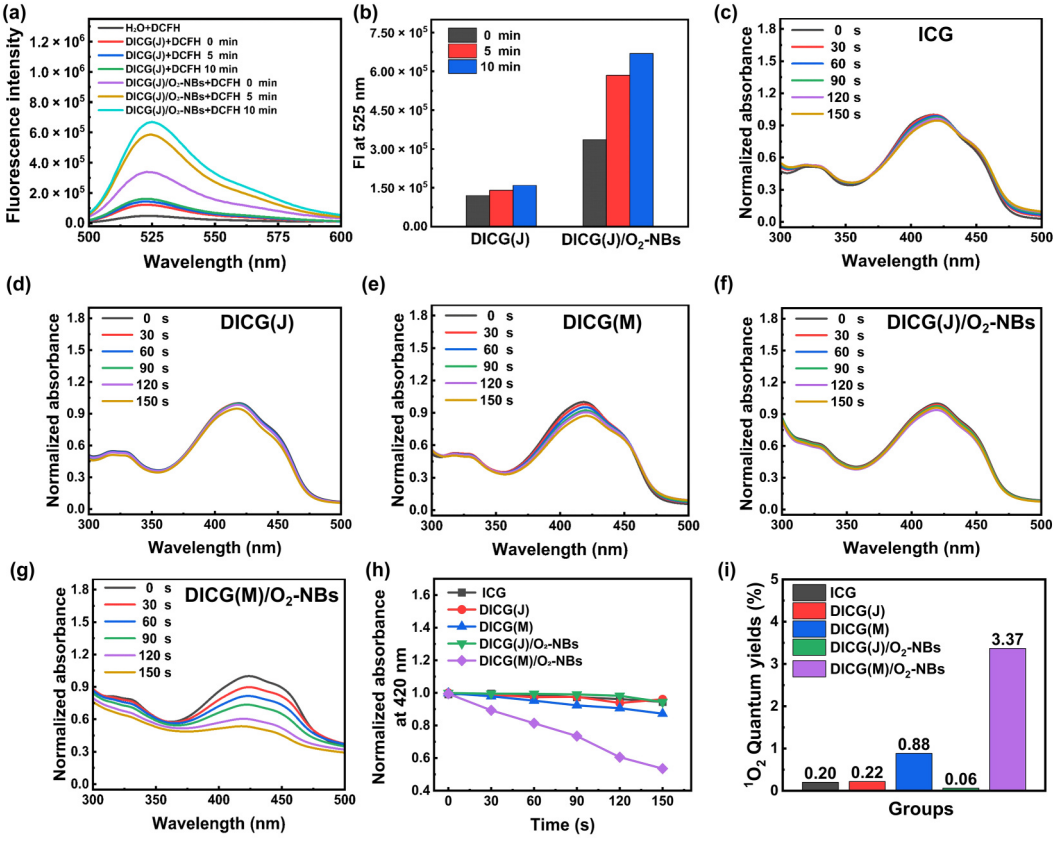

Figure 4 ROS generation of the samples upon irradiation. (a) The fluorescence spectra and (b) fluorescence intensity values at 525 nm of DCFH-H_2O-treated samples. Normalized DPBF degradation induced by (c) ICG, (d) DICG(J), (e) DICG(M), (f) DICG(J)/O_2-NBs, and (g) DICG(M)/O_2-NBs. (h) Normalized DPBF degradation induced by different samples. (i) $^1O_2$ quantum yields of different samples.

3.4 Cellular uptake, cytotoxicity and ROS levels

Inspired by the excellent photothermal and photodynamic properties of DICG(J)/O_2-NBs, a series of cell experiments were carried out to test their *in vitro* PDT and PTT ability. Cal27 cells were incubated with DICG(J) or DICG(J)/O_2-NBs solution with the same DICG concentration (10 μg/mL) for 24 h. The uptake and distribution of DICG(J) and DICG(J)/O_2-NBs in Cal27 cells were observed via CLSM. As shown in Fig. 5(a), DICG(J) was distributed in all the cells except the nucleus, indicating that DICG(J) was efficiently taken up by the tumor cells. The results also revealed that there was no significant difference in the uptake of DICG(J) or DICG(J)/O_2-NBs by Cal27 cells. The cytotoxicity of DICG(J) and DICG(J)/O_2-NBs solution to Cal27 cells was determined via a CCK-8 assay. As shown in Fig. 5(b), in the absence of light, negligible cell cytotoxicity was observed with increasing DICG(J) concentration. Even when Cal27 cells were treated with DICG(J)/O_2-NBs solution with a DICG(J) concentration of 10 μg/mL, the cell viability did not significantly change, highlighting the excellent biocompatibility of DICG(J)/O_2-NBs.

The cell ablation effects of DICG(J) and DICG(J)/O_2-NBs solution under NIR laser irradiation (880 nm, 1 W/cm^2) were also evaluated via a CCK-8 assay. As shown in Fig. 5(c), after treatment with DICG(J) solution plus laser, the activity of Cal27 cells decreased in a dose-dependent manner, which can be attributed to the PTT effect of DICG(J). In particular, DICG(J)/O_2-NBs solution is more toxic to Cal27 cells than DICG(J) solution under laser irradiation, and its ability to kill tumor cells nearly doubles. Compared with that of DICG(J), the significantly increased toxicity of DICG(J)/O_2-NBs is mainly due to self-cascade PTT and PDT effects.

To confirm the effects of cascade PTT and PDT, DCFH-DA was used as an intracellular indicator to evaluate the cellular ROS production of DICG(J) and DICG(J)/O_2-NBs. After the cells were treated with the samples, the green fluorescence was detected via CLSM. In the absence of laser irradiation, as shown in Fig. 5(d), weak fluorescence was detected in the cytoplasm, indicating that the level of ROS production was negligible. Under laser irradiation, the control and O_2-NBs treated groups presented no green fluorescence, whereas the groups treated with DICG(J) and DICG(J)/O_2-NBs presented green fluorescence. Notably, the cells treated with DICG(J)/O_2-NBs solution displayed stronger fluorescence intensity (Fig. S12 in the ESM), indicating that the level of ROS production was significantly greater than that of the DICG(J) solution. The results show that it is feasible to use DICG(J)/O_2-NBs as therapeutic agents for self-cascade PTT and PDT.

3.5 *In vivo* antitumor efficacy

The preliminary *in vitro* results show that DICG(J)/O_2-NBs exhibit considerable potential for self-cascade PTT and PDT. To evaluate the therapeutic ability of DICG(J)/O_2-NBs, their antitumor effects *in vivo* were investigated by establishing a tumor model in nude mice. First, the *in vivo* targeting and enrichment ability of DICG was evaluated. After intravenous injection of DICG solution into the tail vein, the fluorescence signals in the tumor and major organs, such as muscle and liver, were recorded. As shown in Fig. 6(a), the intensity of red fluorescence rapidly increased at the

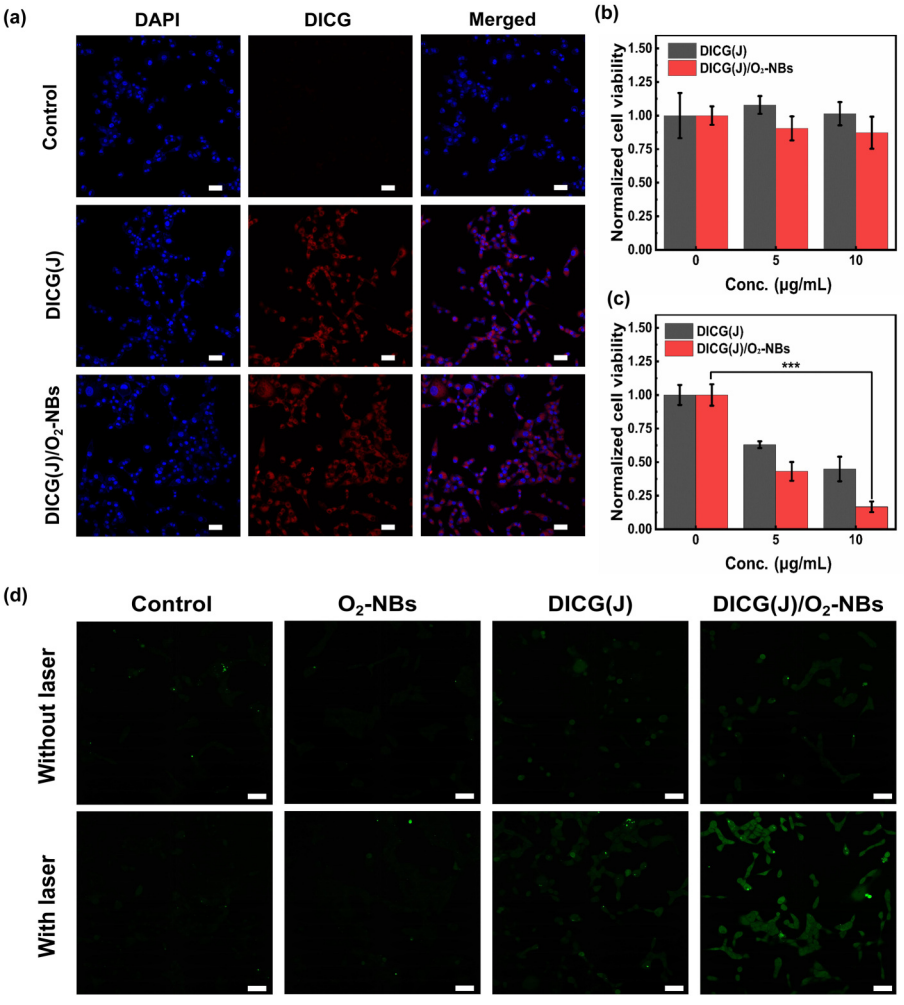

Figure 5 *In vitro* toxicity, cellular uptake, and PTT/PDT experiments with DICG/O_2-NBs. (a) CLSM images of Cal27 cells stained with DAPI after incubation with blank, DICG(J), or DICG(J)/O_2-NBs (DICG, 10 μg/mL). Cell viability profiles of Cal27 cells after treatment with DICG(J) and DICG(J)/O_2-NBs at different DICG concentrations (0, 5, and 10 μg/mL) (b) without laser irradiation and (c) upon laser irradiation (1 W/cm^2, 880 nm). The error bars represent the standard error (mean ± SEM, n = 3). The values are presented as the means ± SEMs, ***P < 0.001. (d) CLSM images of intracellular ROS generation without laser irradiation (top) and after laser irradiation (bottom) (scale bars = 20 μm).

tumor sites, indicating the excellent targeting and enrichment ability of DICG.

The temperature changes in the tumor-bearing mice under NIR laser irradiation were recorded via infrared thermal imaging. In the DICG(J) and DICG(J)/O_2-NBs treatment groups, the maximum temperature of the tumor site reached approximately 46 °C, with a temperature increase of 9 °C after 10 min of laser irradiation (Fig. S13 in the ESM), indicating that DICG(J) and DICG(J)/O_2-NBs have similar PTT effects. After the different treatments were administered, the tumor volume (Fig. S14 in the ESM) and body weight of the mice were recorded every 2 days to evaluate the antitumor effects of the treatments (Figs. 6(b)–6(e)). On day 12, the tumor volume of the control group and DICG(J) group rapidly increased to 3.32 and 4.30 times greater than that on day 1, respectively, indicating that DICG nanoparticles have no inhibitory effect on tumors. However, the relative tumor volume of the DICG(J) plus laser group decreased to 80% of the original volume within 12 days, indicating that DICG(J) has a certain antitumor effect upon laser irradiation. In sharp contrast, the relative tumor volume of the DICG(J)/O_2-NBs plus laser group gradually decreased to 19% of the original volume, suggesting a significant tumor inhibition effect. Similarly, the tumor growth inhibition rates of DICG(J) and DICG(J)/O_2-NBs were calculated to be 76.04% and 94.26% (Fig. S15 in the ESM), respectively.

During the treatments, the oxygen saturation of hemoglobin in Cal27 tumor-bearing nude mice was determined. As shown in Fig. 6(f) and Fig. S16 in the ESM, the oxyhemoglobin (OxyHb) content of the control group did not significantly change. In the DICG(J) plus laser group, the OxyHb mean decreased because of the NIR absorption of DICG(J). In sharp contrast, the OxyHb mean of the DICG(J)/O_2-NBs plus laser group increased remarkably, which can be attributed to the release of oxygen during the PTT procedure. With the switch of therapeutic modes from PTT to PDT, the OxyHb mean decreases slightly, suggesting that the increased oxygen supply of DICG(J)/O_2-NBs is sufficient to guarantee the PDT process.

The above results indicate that DICG(J)/O_2-NBs have a better tumor treatment effect than DICG(J). Compared with that of the DICG(J)/O_2-NBs plus laser group, because the photothermal effect of the DICG(J)/O_2-NBs plus laser group was similar, the difference in the treatment effect was mainly due to the difference in the PDT effect. The PDT effect of the DICG(J)/O_2-NBs laser group was

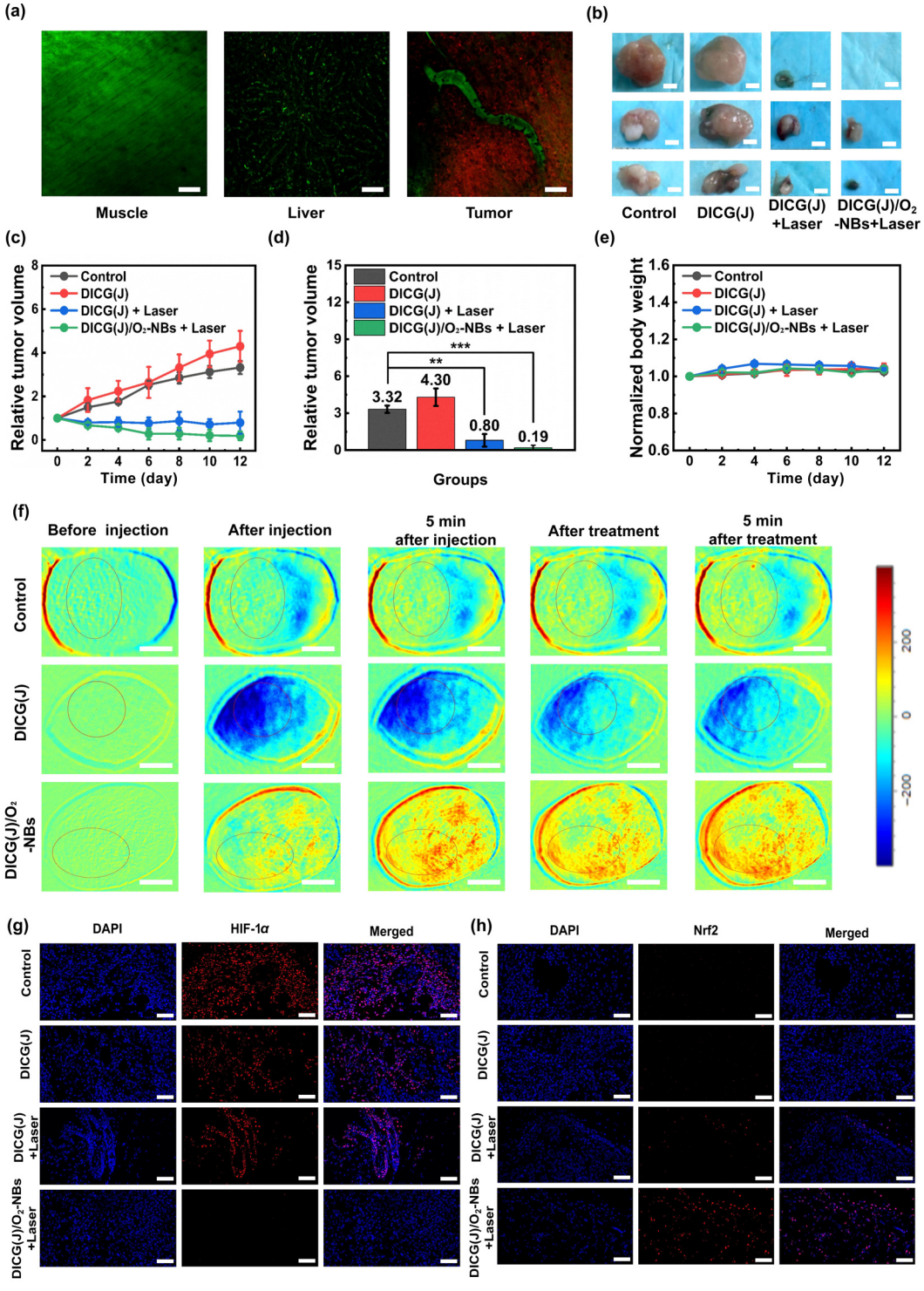

Figure 6 Antitumor efficacy in Cal27 tumor model mice under irradiation with an 880 nm laser. Distribution of (a) DICG (scale bars: 50 μm), (b) tumor photographs (scale bars: 2.5 mm), (c) tumor volume curves, (d) relative tumor volume, (e) Normalized body weight curves, and (f) OxyHb mean photographs (scale bars: 2.5 mm) in tumor-bearing mice. Immunofluorescence of (g) HIF-1*α* and (h) Nrf2 induction factors in the tumors (scale bars: 50 μm). The error bars represent the standard error (mean ± SEM, $n = 3$). The values are presented as the means ± SEMs, $^{**}P < 0.01$, $^{***}P < 0.001$.

significantly improved by increasing the oxygen content in the tumor environment. The extremely high tumor growth inhibition rate of DICG(J)/O_2-NBs can be attributed to self-cascade PTT and PDT *in vitro*.

As shown in Fig. 6(e), there was no significant difference in body weight among the groups within 12 days, which verified the biocompatibility of DICG(J)/O_2-NBs. To further investigate the histocompatibility of DICG(J)/O_2-NBs, after the mice were sacrificed on day 12, the major organs (heart, liver, spleen, lung, and kidney) of each treatment group of mice were resected and collected, and H&E staining was performed. Microscopic observations of H&E-stained sections of all organs from all the mice

revealed no abnormal inflammation or damage (Fig. S17 in the ESM). Furthermore, after DICG(J)/O_2-NBs administration in healthy mice, blood biochemical analysis was performed to obtain a complete count of key blood components. As shown in Fig. S18 in the ESM, there was no significant difference in the hematological indices between the experimental group and the control group. These results demonstrate that DICG(J)/O_2-NBs have good biosafety and reliable therapeutic effects.

3.6 Hypoxia regulation

HIF-1α is a critical factor in tumor adaptation to hypoxic stress. The overexpression of HIF-1α is closely associated with tumor metastasis, angiogenesis, and resistance to therapy [40]. In contrast, Nrf2 is a key transcription factor in the cellular defense against oxidative stress. When cells are attacked by oxidative stress or exogenous toxic substances, Nrf2 is rapidly activated and protects cells through antioxidative mechanisms and other mechanisms [41, 42]. To explore the effects of cascade PTT and PDT, tumor immunofluorescence was performed to analyse HIF-1α and Nrf2 induction factors. As shown in Fig. 6(g), among the four groups, the DICG(J)/O_2-NBs plus laser treatment group presented the weakest immunofluorescence (red) of HIF-1α, indicating that DICG(J)/O_2-NBs successfully improved oxygenation in the tumor microenvironment and inhibited the expression of HIF-1α. On the other hand, the DICG(J)/O_2-NBs plus laser treatment group presented increased expression of Nrf2 (red) in the tumors compared with the other groups (Fig. 6(h)), confirming that a significant amount of ROS was generated during the PDT process. Taken together, these results further verify that the excellent tumor inhibition ability of DICG(J)/O_2-NBs may be due to the effects of self-cascade PTT and PDT.

4 Conclusions

In summary, a light-triggered self-cascade PTT and PDT system, DICG/O_2-NBs, was developed in this work. DICG/O_2-NBs feature typical J-aggregates with significant PTT effects and a high photothermal conversion efficiency of 51.45%. The PTT effects can switch DICG(J) into DICG(M) with efficient O_2 gas liberation and enhanced ·OH and $^1O_2$ production for efficient type I and II PDT. Owing to PTT-cascaded type I and II PDT, DICG/O_2-NBs exhibit high tumor inhibition of 94.26% and obvious hypoxia-reversible capability *in vivo*. Our work demonstrates the efficiency of self-cascade PTT and PDT nanomedicine for high-performance hypoxia-reversible tumor ablation, thus providing a new approach for the development of cascading phototheranostics *in vivo*.

Electronic Supplementary Material: Supplementary material (additional experimental details and data, including ^{1}H NMR spectra of ICG and DICG, the preparation control device of the repeated compression method, nanoparticle concentrations of DICG and DICG(J)/O_2-NBs, fluorescence spectra of the samples, thermal imaging of DICG under different processing conditions, T versus $-\ln(\theta)$ plots for the samples, $\ln(A_0/A)$ at 420 nm versus time plots of the samples, absorbance spectra of the samples, fluorescence intensity of Cal27 cells after being treated with O_2-NBs, DICG(J) and DICG(J)/O_2-NBs upon irradiation, the temperature changes of the irradiation sites with time during the antitumor therapy, the measurement of the tumor volume, the tumor growth inhibition rate of the four groups after various treatments, OxyHb mean photographs and curves of the samples, H&E stained organs of the four groups after various treatments, the serum biochemistry and complete blood panels analysis, and photophysical and photochemical properties of the samples) is available in the online version of this article at https://doi.org/10.26599/NR.2025.94907281.

Data availability

All data needed to support the conclusions in the paper are presented in the manuscript and the Electronic Supplementary Material.

Acknowledgments

This work was supported by the National Key R&D Program of China (No. 2023YFF0713600), the National Natural Science Foundation of China (Nos. 62375138, and 52173135), the National Natural Science Innovative Research Group Project (No. 61821002), the Frontier Fundamental Research Program of Jiangsu Province for Leading Technology (No. BK 20222002), the Natural Science Foundation of Jiangsu Province (No. BK 20231523), and Jiangsu Specially Appointed Professorship.

Declaration of competing interest

The authors declare no competing financial interest.

Author contribution statement

C. W. X., S. L. L., B. H., and N. G. conceived and designed the experiments; X. S., Z. Z., M. R. W, Y. Q. C., X. M., W. J. Z., and W. H. Q. Y. participated in the experiments; X. S, J. J., C. W. X., Y. X. W., S. L. L., and B. H. analyzed the data; S. L. L., B. H., and N. G. wrote the manuscript and supported this study. All the authors provided the final approval of the manuscript.

Informed consent

Not applicable.

Ethics statement

The animal experiments were carried out following the guidelines of the Nanjing Medical University Institutional Committee for the Care and Use of Laboratory Animals and were approved by the Committee on Ethical Use of Animals of Nanjing Medical University (Ethical code: IACUC-2406030).

Use of AI statement

None.

References

[1] Fan, W. P.; Yung, B.; Huang, P.; Chen, X. Y. Nanotechnology for multimodal synergistic cancer therapy. *Chem. Rev.* **2017**, *117*, 13566–13638.

[2] Nguyen, V. N.; Yan, Y. X.; Zhao, J. Z.; Yoon, J. Heavy-atom-free photosensitizers: From molecular design to applications in the photodynamic therapy of cancer. *Acc. Chem. Res.* **2021**, *54*, 207–220.

[3] Pham, T. C.; Nguyen, V. N.; Choi, Y.; Lee, S.; Yoon, J. Recent strategies to develop innovative photosensitizers for enhanced

photodynamic therapy. *Chem. Rev.* **2021**, *121*, 13454–13619.
[4] Xi, D. M.; Xiao, M.; Cao, J. F.; Zhao, L. Y.; Xu, N.; Long, S. R.; Fan, J. L.; Shao, K.; Sun, W.; Yan, X. H. et al. NIR light-driving barrier-free group rotation in nanoparticles with an 88.3% photothermal conversion efficiency for photothermal therapy. *Adv. Mater.* **2020**, *32*, e1907855.
[5] Wu, Z. H.; Peng, M.; Ji, C. D.; Kardasis, P.; Tzourtzouklis, I.; Baumgarten, M.; Wu, H.; Basché, T.; Floudas, G.; Yin, M. Z. et al. A terrylene-anthraquinone dyad as a chromophore for photothermal therapy in the NIR-II window. *J. Am. Chem. Soc.* **2023**, *145*, 26487–26493.
[6] Zhao, M. Y.; Zhuang, H. J.; Li, B. H.; Chen, M. W.; Chen, X. Y. *In situ* transformable nanoplatforms with supramolecular cross-linking triggered complementary function for enhanced cancer photodynamic therapy. *Adv. Mater.* **2023**, *35*, 2209944.
[7] Li, B.; Wang, W.; Zhao, L.; Wu, Y. X.; Li, X. X.; Yan, D. Y.; Gao, Q. X.; Yan, Y.; Zhang, J.; Feng, Y. et al. Photothermal therapy of tuberculosis using targeting pre-activated macrophage membrane-coated nanoparticles. *Nat. Nanotechnol.* **2024**, *19*, 834–845.
[8] Hu, X. M.; Fang, Z. T.; Sun, F. W.; Zhu, C. J.; Jia, M. X.; Miao, X. F.; Huang, L. T.; Hu, W. B.; Fan, Q. L.; Yang, Z. et al. Deciphering oxygen-independent augmented photodynamic oncotherapy by facilitating the separation of electron-hole pairs. *Angew. Chem., Int. Ed.* **2024**, *63*, e202401036.
[9] Melamed, J. R.; Edelstein, R. S.; Day, E. S. Elucidating the fundamental mechanisms of cell death triggered by photothermal therapy. *ACS Nano* **2015**, *9*, 6–11.
[10] Zhang, Y. J.; Zhan, X. L.; Xiong, J.; Peng, S. S.; Huang, W.; Joshi, R.; Cai, Y.; Liu, Y. L.; Li, R.; Yuan, K. et al. Temperature-dependent cell death patterns induced by functionalized gold nanoparticle photothermal therapy in melanoma cells. *Sci. Rep.* **2018**, *8*, 8720.
[11] Jin, Z. Y.; Fatima, H.; Zhang, Y.; Shao, Z. P.; Chen, X. J. Recent advances in bio‐compatible oxygen singlet generation and its tumor treatment. *Adv. Therapeutics* **2022**, *5*, 210076.
[12] Teng, K. X.; Niu, L. Y.; Yang, Q. Z. Supramolecular photosensitizer enables oxygen-independent generation of hydroxyl radicals for photodynamic therapy. *J. Am. Chem. Soc.* **2023**, *145*, 4081–4087.
[13] Teng, K. X.; Chen, W. K.; Niu, L. Y.; Fang, W. H.; Cui, G. L.; Yang, Q. Z. BODIPY-based photodynamic agents for exclusively generating superoxide radical over singlet oxygen. *Angew. Chem., Int. Ed.* **2021**, *60*, 19912–19920.
[14] Chen, H.; Wan, Y. P.; Cui, X.; Li, S. L.; Lee, C. S. Recent advances in hypoxia-overcoming strategy of aggregation-induced emission photosensitizers for efficient photodynamic therapy. *Adv. Healthc. Mater.* **2021**, *10*, e2101607.
[15] Wang, Y.; Luo, S. Y.; Wu, Y. S.; Tang, P.; Liu, J. J.; Liu, Z. Y.; Shen, S. H.; Ren, H. Z.; Wu, D. C. Highly penetrable and on-demand oxygen release with Tumor activity composite nanosystem for photothermal/photodynamic synergetic therapy. *ACS Nano* **2020**, *14*, 17046–17062.
[16] Wilson, B. C.; Weersink, R. A. The Yin and Yang of PDT and PTT. *Photochem. Photobiol.* **2020**, *96*, 219–231.
[17] Overchuk, M.; Weersink, R. A.; Wilson, B. C.; Zheng, G. Photodynamic and photothermal therapies: Synergy opportunities for nanomedicine. *ACS Nano* **2023**, *17*, 7979–8003.
[18] Benítez-Mateos, A. I.; Roura Padrosa, D.; Paradisi, F. Multistep enzyme cascades as a route towards green and sustainable pharmaceutical syntheses. *Nat. Chem.* **2022**, *14*, 489–499.
[19] Lee, M. G.; Li, X. Y.; Ozden, A.; Wicks, J.; Ou, P. F.; Li, Y. H.; Dorakhan, R.; Lee, J.; Park, H. K.; Yang, J. W. et al. Selective synthesis of butane from carbon monoxide using cascade electrolysis and thermocatalysis at ambient conditions. *Nat. Catal.* **2023**, *6*, 310–318.
[20] Du, C.; Mills, J. P.; Yohannes, A. G.; Wei, W.; Wang, L.; Lu, S. Y.; Lian, J. X.; Wang, M. Y.; Guo, T.; Wang, X. Y. et al. Cascade electrocatalysis via AgCu single-atom alloy and Ag nanoparticles in CO_2 electroreduction toward multicarbon products. *Nat. Commun.* **2023**, *14*, 6142.
[21] Cao, W. W.; Zhu, Y.; Wu, F. P.; Tian, Y.; Chen, Z. M.; Xu, W. J.; Liu, S. Y.; Liu, T. T.; Xiong, H. Three birds with one stone: Acceptor engineering of hemicyanine dye with NIR-II emission for synergistic photodynamic and photothermal anticancer therapy. *Small* **2022**, *18*, e2204851.
[22] Jin, T. X.; Cheng, D.; Jiang, G. Y.; Xing, W. Q.; Liu, P. W.; Wang, B.; Zhu, W. P.; Sun, H. T.; Sun, Z. R.; Xu, Y. F. et al. Engineering naphthalimide-cyanine integrated near-infrared dye into ROS-responsive nanohybrids for tumor PDT/PTT/chemotherapy. *Bioact. Mater.* **2022**, *14*, 42–51.
[23] Hu, X. M.; Zhu, C. J.; Sun, F. W.; Chen, Z. J.; Zou, J. H.; Chen, X. Y.; Yang, Z. J-aggregation strategy toward potentiated NIR-II fluorescence bioimaging of molecular fluorophores. *Adv. Mater.* **2024**, *36*, e2304848.
[24] Würthner, F.; Kaiser, T. E.; Saha-Möller, C. R. J-aggregates: From serendipitous discovery to supramolecular engineering of functional dye materials. *Angew. Chem., Int. Ed.* **2011**, *50*, 3376–3410.
[25] Sun, C. X.; Zhao, M. Y.; Zhu, X. Y.; Pei, P.; Zhang, F. One-pot preparation of highly dispersed second near-infrared J-aggregate nanoparticles based on FD-1080 cyanine dye for bioimaging and biosensing. *CCS Chem.* **2022**, *4*, 476–486.
[26] Wei, K.; Wu, Y. X.; Zheng, X.; Ouyang, L.; Ma, G. P.; Ji, C. D.; Yin, M. Z. A light-triggered J-aggregation-regulated therapy conversion: From photodynamic/photothermal therapy to long-lasting chemodynamic therapy for effective tumor ablation. *Angew. Chem., Int. Ed.* **2024**, *63*, e202404395.
[27] Liu, R. F.; Tang, J.; Xu, Y. X.; Zhou, Y. M.; Dai, Z. F. Nano-sized indocyanine green J-aggregate as a one-component theranostic agent. *Nanotheranostics* **2017**, *1*, 430–439.
[28] Vincy, A.; Bhatia, N.; Vankayala, R. Optical characteristics of indocyanine green J-aggregates induced by cisplatin for phototheranostic applications. *ACS Biomater. Sci. Eng.* **2022**, *8*, 5119–5128.
[29] Bhavane, R.; Starosolski, Z.; Stupin, I.; Ghaghada, K. B.; Annapragada, A. NIR-II fluorescence imaging using indocyanine green nanoparticles. *Sci. Rep.* **2018**, *8*, 14455.
[30] Sun, X. Y.; Xu, Y.; Guo, Q. K.; Wang, N.; Wu, B.; Zhu, C.; Zhao, W.; Qiang, W. L.; Zheng, M. A novel nanoprobe for targeted imaging and photothermal/photodynamic therapy of lung cancer. *Langmuir* **2022**, *38*, 1360–1367.
[31] Lin, H. R.; Zhou, Y.; Wang, J. M.; Wang, H. M.; Yao, T. H.; Chen, H.; Zheng, H. L.; Zhang, Y.; Ren, E.; Jiang, L. et al. Repurposing ICG enables MR/PA imaging signal amplification and iron depletion for iron-overload disorders. *Sci. Adv.* **2021**, *7*, eabl5862.
[32] Kwon, N.; Jasinevicius, G. O.; Kassab, G.; Ding, L. L.; Bu, J. C.; Martinelli, L. P.; Ferreira, V. G.; Dhaliwal, A.; Chan, H. H. L.; Mo, Y. L. et al. Nanostructure-driven indocyanine green dimerization generates ultra-stable phototheranostics nanoparticles. *Angew. Chem., Int. Ed.* **2023**, *62*, e202305564.
[33] McEwan, C.; Owen, J.; Stride, E.; Fowley, C.; Nesbitt, H.; Cochrane, D.; Coussios, C. C.; Borden, M.; Nomikou, N.; McHale, A. P. et al. Oxygen carrying microbubbles for enhanced sonodynamic therapy of hypoxic tumours. *J. Control. Release* **2015**, *203*, 51–56.
[34] Huang, B.; Yang, L.; Yu, W. B.; Li, Y.; Li, L.; Gu, N. Advances of therapeutic microbubbles and nanobubbles. *Nat. Sci. Open* **2023**, *2*, 20220062.
[35] Song, L.; Wang, G. H.; Hou, X. D.; Kala, S.; Qiu, Z. H.; Wong, K. F.; Cao, F.; Sun, L. Biogenic nanobubbles for effective oxygen delivery and enhanced photodynamic therapy of cancer. *Acta Biomater.* **2020**, *108*, 313–325.
[36] Yang, L.; Huang, B.; Hu, S. Q.; An, Y.; Sheng, J. Y.; Li, Y.; Wang, Y. X.; Gu, N. Indocyanine green assembled free oxygen-nanobubbles towards enhanced near-infrared induced photodynamic therapy. *Nano Res.* **2022**, *15*, 4285–4293.

[37] Rüttger, F.; Mindt, S.; Golz, C.; Alcarazo, M.; John, M. Isomerization and dimerization of indocyanine green and a related heptamethine dye. *Eur. J. Org. Chem.* **2019**, *2019*, 4791–4796.

[38] Jin, J.; Feng, Z. Q.; Yang, F.; Gu, N. Bulk nanobubbles fabricated by repeated compression of microbubbles. *Langmuir* **2019**, *35*, 4238–4245.

[39] Zhao, X. Z.; Long, S. R.; Li, M. L.; Cao, J. F.; Li, Y. C.; Guo, L. Y.; Sun, W.; Du, J. J.; Fan, J. L.; Peng, X. J. Oxygen-dependent regulation of excited-state deactivation process of rational photosensitizer for smart phototherapy. *J. Am. Chem. Soc.* **2020**, *142*, 1510–1517.

[40] Chen, F.; Chen, J. N.; Yang, L. B.; Liu, J.; Zhang, X. Q.; Zhang, Y.; Tu, Q. Q.; Yin, D.; Lin, D. C.; Wong, P. P. et al. Extracellular vesicle-packaged HIF-1α-stabilizing lncRNA from tumour-associated macrophages regulates aerobic glycolysis of breast cancer cells. *Nat. Cell Biol.* **2019**, *21*, 498–510.

[41] Rojo De La Vega, M.; Chapman, E.; Zhang, D. D. NRF2 and the hallmarks of cancer. *Cancer Cell* **2018**, *34*, 21–43

[42] Qin, C.; Yang, S.; Chu, Y. H.; Zhang, H.; Pang, X. W.; Chen, L.; Zhou, L. Q.; Chen, M.; Tian, D. S.; Wang, W. Signaling pathways involved in ischemic stroke: Molecular mechanisms and therapeutic interventions. *Signal Transduct. Target. Ther.* **2022**, *7*, 215.